J. Fluid Mech. (2000), *vol.* 417, *pp.* 47–75. Printed in the United Kingdom

Flow physics of discrete boundary layer suction – measurements and predictions

By D. G. MacMANUS† AND J. A. EATON

Aerospace Research Centre, National University of Ireland, Galway, Ireland

(Received 17 October 1997 and in revised form 23 March 2000)

The primary objective of this work is to determine the detailed characteristics of the flow features induced in a boundary layer by suction through laminar flow control (LFC) perforations. An additional goal is to validate a predictive method for generic LFC suction surfaces and to apply this technique to typical flight condition configurations. Fundamental insights into the flow physics of LFC suction surfaces are obtained from a unique series of high-resolution three-component laser Doppler velocimetry (LDV) flow field measurements. The flow fields induced by isolated super-scale perforations under low-speed conditions are mapped and found to be strongly three-dimensional and profoundly different from the idealized concept of continuously distributed suction. Over a range of sub- and super-critical suction flow rates a variety of suction-dependent complex flow features are identified, including a pair of contra-rotating streamwise vortices, multiple co-rotating streamwise vortices, spanwise variations of the mean flow and inherently unstable boundary layer profiles. The measurements reveal that suction-induced transition commences with an instability of these attached vortices, resulting in the development of a pair of turbulent wedges downstream of the perforation. A finite-volume Navier–Stokes method is validated by simulating a variety of low-speed experiments and comparisons are made between the LDV measurements and the predicted flow field. The computational technique reproduces all of the observed flow features, although it slightly under-predicts their magnitude and extent. By analysing the predicted flow fields the mechanism for the formation of the trailing vortex pair is established. Earlier flow visualization experiments, which exhibited vortex shedding, are also simulated by solving the time-dependent governing equations and it is found that the principal unsteady flow features are captured. Despite the challenge posed to the computational method by the diverse range of flow phenomena induced by discrete suction, the predictions provide good agreement with the measurements and observations. The computational tool is subsequently applied to predict the flow fields of single and multiple rows of actual-scale micro-perforations under low-speed and typical transonic flight conditions. A range of suction-induced flow features are predicted and a variety of distinct flow modes are identified. The low-speed critical suction limits are also measured and a design criterion, based on the sucked streamtube characteristics, is established. The basis of this critical suction criterion is also validated for transonic flight configurations.

---

† Present address: Rolls-Royce plc, P.O. Box 31, Derby, DE24 8BJ, UK.

1. Introduction

The application of laminar flow control (LFC) technology to large transport aircraft is an attractive way to reduce drag under transonic cruise conditions (Saric 1985; Arnal 1992). LFC reduces the skin friction drag, which accounts for up to 50% of total drag at cruise (Holmes 1987*a*, *b*), by stabilizing the boundary layer and moving the transition location as far aft as possible. Contemporary thinking suggests that for wing and tail surfaces the laminar boundary layer is best stabilized using hybrid laminar flow control (HLFC). HLFC uses a combination of surface suction, applied in the leading-edge region, and favourable pressure gradients, attained by wing profile shaping (Pfenninger 1977; Arnal 1992). Surface suction stabilizes the boundary layer via two mechanisms. The primary effect is to alter the mean velocity distribution to produce a fuller, more stable, velocity profile and a weaker secondary effect decreases the overall boundary layer thickness, thereby reducing the associated Reynolds number, Re_{δ^*}. In addition to satisfying aerodynamic constraints, realization of surface suction is determined by manufacturing capabilities, by structural criteria and by operational considerations. Many different designs to implement optimum surface suction have been assessed (Braslow & Fischer 1984) and current HLFC design philosophy is to apply discrete suction through numerous laser-drilled micro-perforations. These perforations are typically 50 μm in diameter and are arranged in a staggered configuration with a pitch to diameter ratio of about 10.

Although the application of discrete suction through micro-perforations is capable of delaying boundary layer transition, the physical details of how, and to what extent, concentrated suction perturbs and changes the local and downstream flow field are largely unknown. At the most fundamental level, the flow field induced by an array of HLFC suction perforations may be expected to be of a three-dimensional nature, very likely strongly so, and considerably different from the idealized concept of continuously distributed suction (Goldsmith 1957; Gregory 1961, 1962; Saric 1985). Moreover, one may anticipate the presence of a variety of complex features: for instance, trailing streamwise vortices, non-uniformity of the mean flow, strong crossflow velocities, unsteady flow structures and local streamline curvature (figure 1). It is important to establish whether such features arise for HLFC perforations, because any of these phenomena will influence the stability of the laminar boundary layer and may, under certain circumstances, expedite rather than delay the onset of transition (Nayfeh 1981; Saric 1985; Herbert 1988; Reed & Saric 1989). Although the application of low suction levels can have a favourable effect on the boundary layer stability, an upper limit exists beyond which an increase in the suction level destabilizes the flow and causes premature transition (Goldsmith 1957; Gregory 1961, 1962; Reneaux & Blanchard 1992). This limit is called the critical suction velocity ratio, $(V_h/U_e)_{crit}$, where V_h is the average suction velocity through the perforation and U_e is the streamwise velocity at the boundary layer edge.

The present study addresses the lack of knowledge and understanding of the flow field induced by suction through micro-perforations in a laminar boundary layer. The primary objectives of this work are to determine the extent and characteristics of the flow features induced by a HLFC suction perforation and to validate a predictive tool for assisting in the design of generic HLFC suction surfaces. Results from the application of this computational method to real-scale suction surfaces under flight conditions are also presented. A further objective is to demonstrate the application of innovative, non-intrusive measurement techniques to reveal the detailed flow field of small-scale highly sensitive flows.

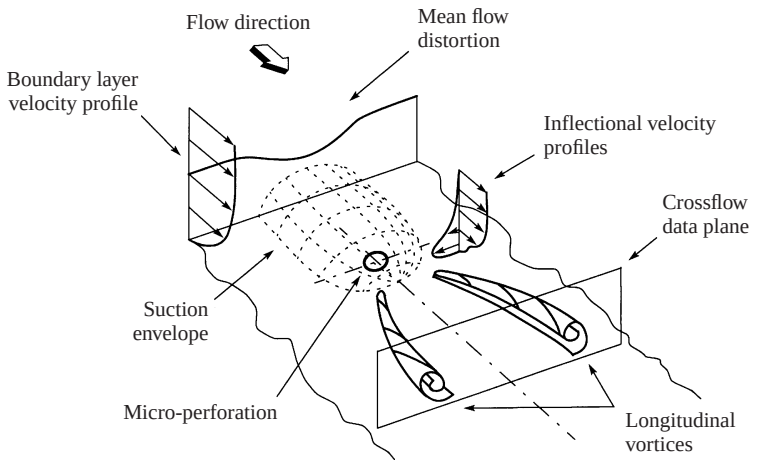

FIGURE 1. Schematic of the flow field induced by a HLFC suction perforation.

The flow fields induced by isolated super-scale HLFC suction perforations are mapped using a non-intrusive high-resolution velocity measurement technique. In parallel with these measurements, a series of Navier–Stokes simulations are conducted to predict the suction-induced flow fields and comparisons are made between the measured and computed velocity fields. Further validation of the prediction technique is achieved by simulating earlier flow visualization experiments (Gregory 1962) which revealed unsteady phenomena generated by suction through a row of closely spaced super-scale perforations. The measurements also determine the critical suction limits and an engineering design criterion for critical suction is established. Results from the application of the computational method to real-scale suction surfaces under flight conditions are also presented.

2. Experiment design

Owing to the prohibitively microscopic scale, in the order of tens of microns, of actual HLFC suction perforations, there are no detailed measurements of the flow field induced by discrete suction under flight conditions. The difficulties posed are illustrated in figure 2, where the size of an actual LFC suction perforation is compared to that of a typical miniature hot-wire probe. Conventional measurement techniques are unable to provide sufficient spatial resolution, and the only feasible solution was to scale up the perforation size so that the velocity distributions could be determined using a high-resolution laser Doppler velocimetry (LDV) system.

Neglecting pressure gradient effects, a dimensional analysis reveals that the appropriate dimensionless groups include: the ratio of perforation diameter to boundary layer displacement thickness, d/δ^*; the ratio of average suction velocity through the perforation to boundary layer edge velocity, V_h/U_e; the displacement thickness Reynolds number, $Re^*_\delta(= U_e\delta^*/\nu)$; the ratio of perforation depth to perforation diameter, L/d; the suction perforation Reynolds number, $Re_d(= V_h d/\nu)$; the unit Reynolds number, $Re'(= U_e/\nu)$ and the Mach number, M_∞. To ensure that the flow field induced by a super-scale perforation exhibits the same features as those of an actual HLFC suction perforation, dynamic similarity is required. Consequently, a group of super-scale (of the order 20 : 1), low-speed experiments were designed in which the parameters d/δ^*, V_h/U_e, Re^*_δ, L/d, and Re_d were preserved. This gave a

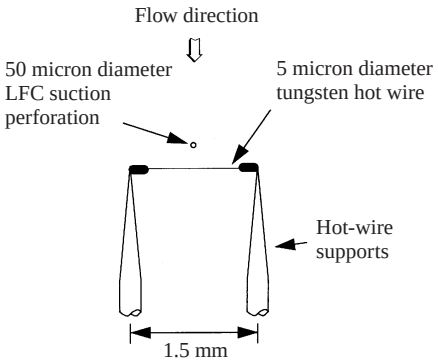

FIGURE 2. Comparison between the size of a HLFC perforation and a typical hot-wire probe.

perforation diameter which is still very small ($d \approx 1$ mm), and for micro-scale flow field measurements in a sensitive laminar boundary layer (where the issue of transition is of fundamental interest) it is crucial that the technique used is non-intrusive. For this reason a three-component, high-resolution LDV was selected. Although the unit Reynolds number and Mach number of the experiment did not match those under flight conditions, and the influence of an array of perforations was neglected, it was anticipated that all of the primary effects of applying discrete suction through micro-perforations would be captured.

The flow fields induced by isolated, super-scale perforations were examined for both sub- and super-critical suction configurations (V_h/U_e varied from 0.15 to 2.0). For an isolated perforation, one of the most important parameters is d/δ^*; preservation of d/δ^* was therefore given priority when designing these experiments. Three super-scale perforations were studied ($d = 0.8$ mm, 1.0 mm and 1.3 mm), providing a range of d/δ^* between 0.68 and 1.05. The perforation ducts were cylindrical, perpendicular to the wall, and of equal length (16.4 mm), which gave an L/d range between 12.6 and 20.5. The free-stream speeds were set nominally between 12 m s^{-1} and 16 m s^{-1}.

3. Experimental apparatus and procedure

3.1. *Wind tunnel model*

The experiments were performed in a low-speed, low-turbulence wind tunnel at the Department of Aerospace Engineering at Bristol University. The working section is 0.8 m $\times$ 0.6 m and the free-stream turbulence level is less than 0.1% at the operating speeds used here (Barrett 1984). The model is a purpose-built aluminium flat plate, 1450 mm long $\times$ 795 mm wide $\times$ 25.4 mm thick, with an elliptical leading-edge profile and an adjustable trailing-edge flap. The model surface was carefully hand polished to reduce surface roughness. Three suction perforations were located on the upper surface 450 mm from the leading edge. Static pressure tappings (0.5 mm bore) were positioned on the upper surface, 12 on each side, 80 mm from the plate edge. The trailing-edge flap was adjusted to provide a stable boundary layer, and the static pressure along the plate was monitored using an inclined manometer. The plate and flap were adjusted until the static streamwise pressure gradient was nominally zero and symmetric about the streamwise axis. 'Natural' and suction-induced transition was monitored using a miniature flush-mounted hot-film sensor element (TSI model 1628) positioned 180 mm downstream of the suction perforations. The perforations

were connected, one at a time, to the suction system, and the flow rate was set and controlled using an electronic mass flow controller (Omega FMA 1416). Both hot-wire anemometer and LDV measurements independently verified that the flow at the perforation inlet was steady, as desired, and that no perturbations from the suction system reached the surface.

3.2. *LDV measurement system*

The LDV system consisted of a 5 W argon-ion laser (Spectra Physics Stabilite 2016), a transmitter box (Dantec model 60X40), two fibre-linked optic heads, a three-axis traverse mechanism and three Dantec Burst Spectrum Analysers (model 57N10). The Dantec fibre optic system included a two-component probe head (Dantec model 60X17), with two pairs of orthogonal beams, green (wavelength, $\lambda = 514.5$ nm) and blue ($\lambda = 488.0$ nm), and a one-component probe head (Dantec Model 60X16) with a pair of violet beams ($\lambda = 476.5$ nm). The system was operated in the off-axis mode, which has the effect of reducing the measurement volume to a sphere of approximately 80 μm diameter for a focal length of 600 mm. This measurement volume size is based on the transit distance (average transit time × velocity). The six beams were carefully aligned using the pin-hole meter procedure developed at the University of Bristol (Barrett *et al.* 1993), thus enabling measurements to be obtained down to approximately 50 μm from the surface.

3.3. *Instrumentation and measurement uncertainty*

Sources of uncertainty due to the model geometry, suction system and LDV were identified and analysed and their influence on the overall data fidelity was assessed. Uncertainties associated with the LDV system include: positional accuracy, gradient bias, velocity bias, statistical errors due to finite sample size, optical uncertainties, alignment uncertainties, calibration and transformation errors, particle behaviour, and frequency measurement (MacManus *et al.* 1996). A detailed analysis of these uncertainty sources and of their influence on the measurements is reported by MacManus (1997). The inter-dependent nature of the various sources of uncertainty, both systematic and random, makes estimation of the overall uncertainty difficult. Simply to quote a maximum error for the measurements, such as occurs at the vortex cores where the positional error is substantial ($\sim 1\%$), would be quite misrepresentative of the majority of the flow field. Therefore the estimated errors at two characteristic positions ('best' case and 'worst' case) within the flow field are indicated. By simply summing these individual components it could be concluded that the peak overall uncertainties in the mean velocities are of the order of 0.5% in the free stream and less than 2.0% in the highly vortical regions.

4. Measurements

The objective of these experiments is to reveal, by mapping the velocity field, a detailed description of how a HLFC suction perforation affects a laminar boundary layer. Measurements of the three velocity components were taken on crossflow data planes normal to the free-stream direction, both upstream and downstream of the perforation centre (1d upstream and 1d, 3d, 5d and 8d downstream of the perforation). On a typical crossflow plane (8 mm × 4 mm) up to 550 data points were used. Three-dimensional boundary layer velocity profiles were acquired at various locations up to 123d downstream of the perforation. These mean velocity profiles were taken both along the perforation longitudinal centreline and also at off-centre locations

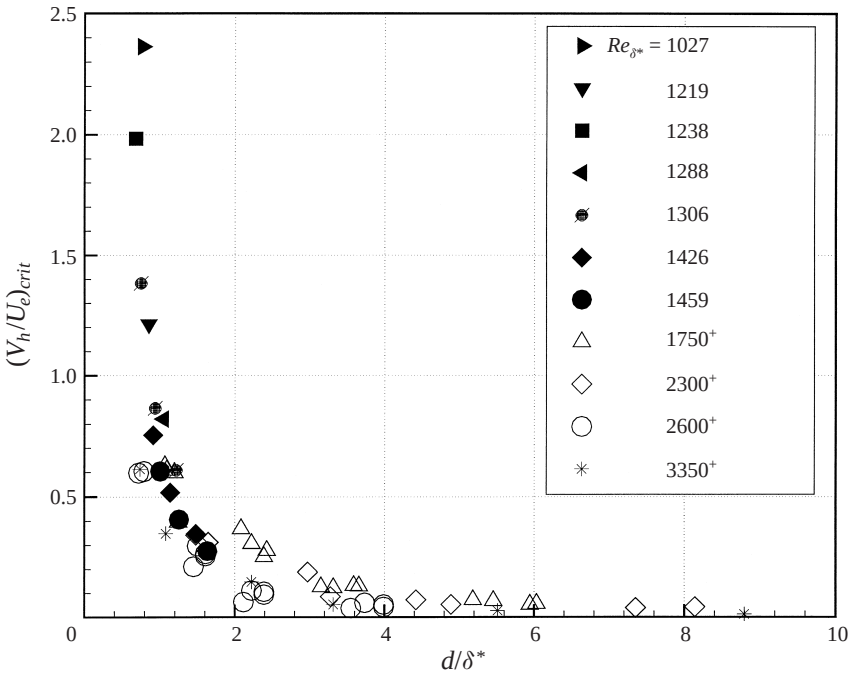

FIGURE 3. Variation of critical suction velocity ratio, $(V_h/U_e)_{crit}$, with d/δ^*. Comparison between the current low-speed experiments and previous transonic measurements (+) by Blanchard *et al.* (1991).

coincident with one of the streamwise vortex cores which were found to occur aft of the perforation. The critical suction velocity ratio for each perforation, over a range of free-stream speeds, was determined using the flush-mounted hot-film sensor. Also, to monitor the boundary layer state and the transition process over an extended area, the r.m.s. velocity was measured on planes parallel to the plate surface.

5. Experimental observations

Although the application of suction through micro-perforations can stabilize the boundary layer, there exists a limit beyond which an increase in the suction speed will destabilize the flow and cause transition. The current series of experiments revealed the critical suction limits and comparisons are made with previous transonic results. With suction applied a variety of flow features were observed, notably: a single pair of contra-rotating streamwise vortices, multiple pairs of co-rotating streamwise vortices, distortions of the streamwise and crossflow velocity profiles, and a pair of turbulent wedges far downstream of the perforation when super-critical suction is applied.

5.1. *Suction-induced transition*

For HLFC design purposes it is important to determine the critical suction limits and to this end gradually increasing suction was applied while the state of the boundary layer was monitored using the hot-film sensor. Output from the sensor revealed that the transition process commenced with the growth of regular Tollmien–Schlichting type oscillations, which was followed by increasing levels of intermittency and finally by a fully turbulent flow. For ease of identification, transition was deemed to occur at the first intermittent signal and the suction-induced transition process was monitored

over a range of free-stream velocities between $12.2\,\mathrm{m\,s^{-1}}$ and $28.4\,\mathrm{m\,s^{-1}}$. In figure 3 the critical suction velocity ratio, V_h/U_e, is plotted against d/δ^* for the current low-speed tests as well as for previous transonic cases. As can be seen, the results are grouped together well, and the critical suction velocity ratio is shown to increase as d/δ^* decreases. This plot also indicates that, as d/δ^* is decreased, there may be a limit below which suction does not precipitate transition ($d/\delta^* < 0.6$). This is an important finding and underlines the potential benefits of using even smaller holes. Although there is much uncertainty concerning the maximum allowable suction rate for HLFC perforated surfaces, current design philosophy employs an upper limit of approximately $50\,\mathrm{m\,s^{-1}}$ on the suction velocity, V_h, at cruise conditions. A simple corollary of figure 3, obviously ignoring compressibility and the effects of multiple holes, is that this restriction is too severe for the all-important leading-edge region of a typical HLFC configuration ($d \approx 50\,\mu\mathrm{m}$, $d/\delta^* \approx 1.0$, $M_\infty \approx 0.8$). Although previous experimental investigations have studied configurations with d/δ^* up to about 10, the current tests have focused on the more relevant region of $0.68 < d/\delta^* < 1.63$.

5.2. *Contra-rotating streamwise vortices*

The most prominent feature to develop is a pair of contra-rotating streamwise vortices trailing behind each perforation. A typical example of the evolution of these streamwise vortices is shown in figure 4, where the V, W velocity vectors are plotted in a sequence of crossflow data planes from $1d$ upstream to $8d$ downstream, for a 1.3 mm perforation with sub-critical suction applied. Downstream of the perforation the spanwise, or lateral, spacing of the vortices increases and the vortex centre (hereafter referred to as the core) moves away from the surface. Immediately aft of the perforation the spanwise spacing grows appreciably, but further downstream the vortices become more closely aligned with the free-stream direction and remain close to the surface (at $8d$ downstream the vortex cores are typically spaced about $4d$ apart and lie approximately $0.5d$ from the plate surface). The lateral spacing of the longitudinal vortex pair also grows as the suction flow rate is increased.

5.3. *Multiple streamwise vortices*

When high, though not necessarily critical, suction flow rates are applied, there is a marked difference in the vortices that are generated downstream of the perforation. Instead of a single pair of contra-rotating streamwise vortices, four vortices appear: a pair of co-rotating vortices on each side of the centreline. The appearance of these secondary vortices outboard of the primary pair has also been previously observed (Meyer 1955) using smoke visualization. In the present investigation, these secondary, co-rotating vortices were observed for both sub- and super-critical suction velocities. Owing to the locally large crossflow velocities induced by the suction perforation, the occurrence of these co-rotating vortices is similar to the formation of boundary layer vortex structures in crossflow-dominated flows. The measurements reveal that the co-rotating vortices are still evident $8d$ downstream of the perforation and a typical plot at $3d$ downstream is shown in § 7.1, where a comparison is made between the experimental and numerical results.

5.4. *Boundary layer profiles*

Wall suction stabilizes the flow via two mechanisms. It decreases the boundary layer thickness, thereby reducing Re_{δ^*}, and it improves the stability characteristics of the streamwise velocity profile. The thinning of the boundary layer and the associated decrease in the curvature term, $\partial^2 U/\partial y^2$, is borne out by the observed deflection of

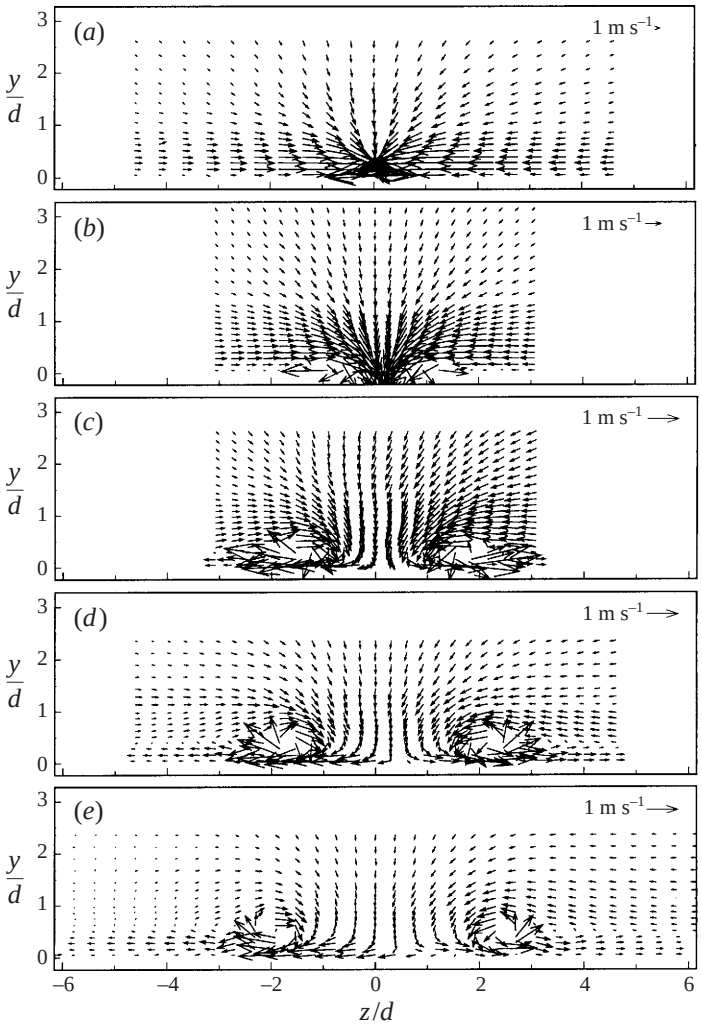

FIGURE 4. Sequence of measured V, W velocity vectors in crossflow data planes upstream and downstream of an isolated perforation with sub-critical suction applied: (*a*) $x/d = -1$, (*b*) 1, (*c*) 3, (*d*) 5, (*e*) 8 ($d = 1.3$ mm, $d/\delta^* = 1.05$, $V_h/U_e = 0.58$).

the measured U velocity contours, both upstream and downstream of the perforation (figure 5). In the region downstream of the perforation, the spanwise extent of this effect is bounded by the spacing of the streamwise vortices. These suction-induced local non-uniformities of the mean flow result in inflectional spanwise velocity profiles and may produce a perturbation effect analogous to a surface roughness element, and thereby increase the susceptibility of the boundary layer to external disturbances (Morkovin 1978). Off the perforation centreline, however, the boundary layer profiles are highly distorted. An example of the streamwise velocity profiles at five stations along the core of one of the vortices is shown in figure 6. The retardation of the streamwise velocity at the vortex centre produces unstable, inflectional velocity profiles. Also evident in these streamwise velocity profiles is the evolution of the streamwise vortex. As it progresses downstream of the perforation the vortex diffuses and its core migrates away from the surface.

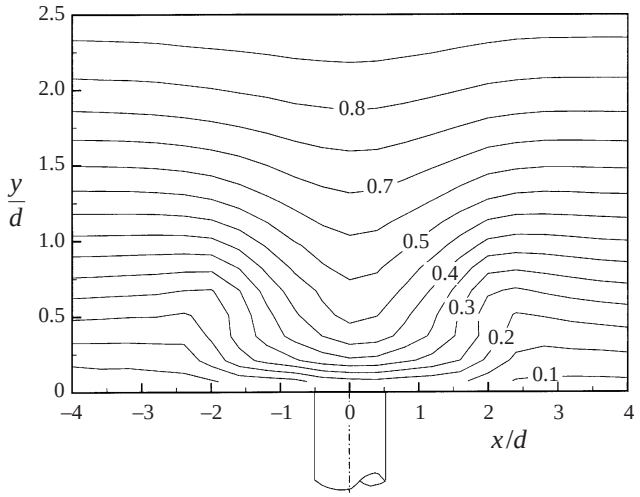

FIGURE 5. Facing upstream, contours of streamwise velocity, U/U_e, on a crossflow data plane $8d$ downstream of an isolated perforation with sub-critical suction applied (Case I, $d = 1.0$ mm, $d/\delta^* = 0.77$, $V_h/U_e = 0.50$ – Cases are listed in table 1, § 6).

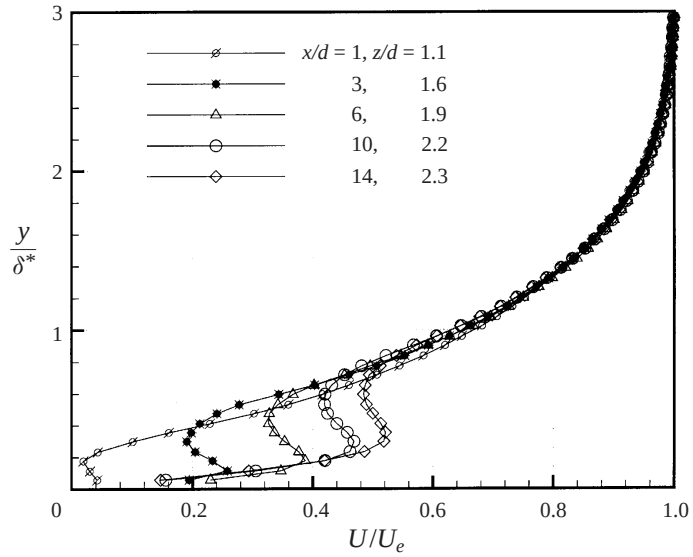

FIGURE 6. Streamwise velocity profiles measured along the track of a longitudinal vortex with super-critical suction applied (Case II, $d = 1.3$ mm, $d/\delta^* = 1.05$, $V_h/U_e = 1.02$).

5.5. *Laminar–turbulent transition mechanism*

Using the LDV in single-component mode, the r.m.s. velocity of an approximately streamwise component was measured in extensive planes parallel to the surface. These horizontal scans were taken at 0.1 mm, 0.4 mm and 0.5 mm height and the surveyed area extended from 5.0 mm upstream to 160.0 mm downstream of the perforation centre. Two typical scans, taken at 0.1 mm ($y/\delta^* = 0.08$) and 0.5 mm ($y/\delta^* = 0.40$) from the surface, for a super-critical suction flow rate, are presented in figure 7. Downstream of $x/d \approx 10$ the scan planes lie below the vortex cores, and the flow is considered to be turbulent when the r.m.s. velocity is greater than approximately

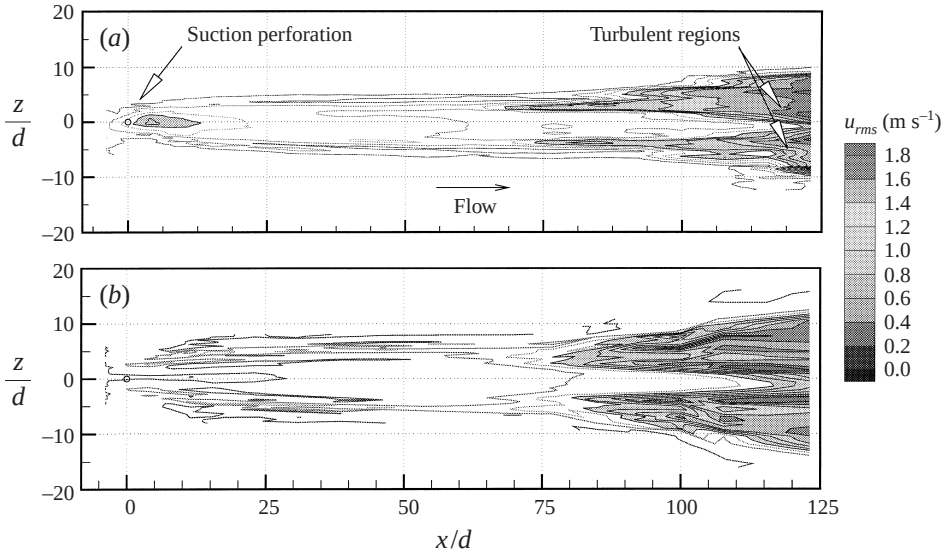

FIGURE 7. Horizontal scans, taken close to the surface, of (approximately) streamwise r.m.s. velocity component fluctuations showing inception and evolution of the pair of turbulent wedges which form downstream of a suction perforation with super-critical suction applied (Case II, $d = 1.3$ mm, $d/\delta^* = 1.05$, $V_h/U_e = 1.02$). Distance from surface (*a*) 0.1 mm; (*b*) 0.5 mm.

1.0 m s^{-1}. For this case, in each scan the development of two turbulent regions (begining at about $x/d = 75$), positioned symetrically about the centreline, can be clearly seen. These regions are where the trailing streamwise vortices become unstable and precipitate transition. The total included angle of the pair of turbulent regions at both heights is about 15°. In figure 7(*a*) the scan is very close to the wall, and the turbulence level increases rapidly to form the characteristic twin wedges. The scan in figure 7(*b*) lies about halfway between the vortex core and the wall. Within each turbulent region the vortex core is bordered by distinct ridges of peak turbulence. Based on a series of similar images it appears that the instabilities are initiated on a slender conical surface that surrounds each vortex core. These disturbances grow and merge until a single fully turbulent wedge is formed. In conclusion, the suction-induced transition process is initiated by instabilities in the streamwise vortices, which ultimately transition and coalesce to form a turbulent wedge.

Because of the off-centre, symmetric location of the turbulent regions, the initial signs of transition may pass undetected on each side of the hot-film sensor (which was positioned on the centreline) and therefore the critical suction velocity ratios presented in § 5.1 may be slightly overestimated.

6. Computational predictions

One of the objectives of this work is to develop a validated prediction technique for HLFC suction surfaces. In practice, the actual laser-drilled perforations have irregular geometries and under flight conditions the flow field is highly three-dimensional, subject to compressibility and viscous effects, and may be unsteady. A numerical procedure has been developed to analyse isolated holes as well as single and multiple rows of perforations under both low-speed and transonic conditions (MacManus & Eaton 1996*a*, *b*; MacManus 1997). The computational method is capable of modelling

the compressible laminar time-dependent Navier–Stokes equations. The current wind tunnel LDV measurements, along with previous flow visualization results (Gregory 1962), are used to provide a range of test cases for validating the method. First, a group of isolated perforation configurations from the present experiments are treated in steady state (§ 6.2). Second, one of Gregory's flow visualization experiments on a single transverse row of perforations, where vortex shedding was observed, is modelled in time-dependent form (§ 6.3). Subsequent to these validation tests the method is applied to a variety of wind-tunnel and flight-condition configurations.

6.1. *Numerical method*

Owing to the large length scales ($O(10^4\delta^*)$) that occur from the onset of instability to flow breakdown and the enormous disparity in the disturbance amplitudes involved in the transition process ($O(e^{10})$ – a ratio of about $10^4:1$), the modelling of flow breakdown demands prodigious computer resources and is currently limited to simple flows and geometries. Although the complete laminar Navier–Stokes equations are solved here, the domain size as well as temporal and spatial resolutions are insufficient to simulate the transition process. Consequently, this computational work does not attempt to model transition induced by discrete suction.

The computational domain was discretized on a body-fitted, multi-block structured grid and the finite-volume method was used to solve the governing equations on a generalized curvilinear coordinate system (CFDS 1994). All terms in the governing equations, apart from the advection terms and the convection coefficients, were spatially discretized using second-order centered differencing. The advection terms were discretized by applying a third-order quadratic upwind scheme (QUICK) as detailed by Leonard (1979). The convection coefficients were obtained using the Rhie–Chow interpolation method (Rhie & Chow 1983) and the SIMPLEC algorithm was used for the pressure-correction equation (Van Doormal & Raithby 1984). Owing to the complex, multi-block grid structure and the low proportion of well-ordered blocks an algebraic multi-grid method was used to solve the linearized difference equations for velocity and pressure. Enthalpy was treated, on a block by block basis, using Stone's strongly implicit procedure.

Five types of boundary conditions were used: symmetry, pressure, mass flow, inlet, and walls (figure 8). On symmetry planes, the normal velocity was set to zero and zero normal gradient was applied to all variables. Pressure boundaries used Dirichlet conditions imposed on pressure and Neumann conditions on velocity. The treatment of the other variables depended on whether the flow is passing into or out of the boundary. To minimize any induced errors, the top, side and downstream faces of the domain, where uniform ambient pressure was prescribed, were located far away from the perforation. Flow through the suction hole was enforced by specifying the mass flow rate which passes out of the domain at the perforation outlet.

6.2. *Isolated perforations – steady-state simulations*

Three of the experimentally investigated configurations described and reported in § 2 to § 5 were simulated as part of the validation procedure for the computational method (Cases I–III in table 1). Because the experiments were conducted at low speeds and only steady flow features were observed, the flow field was assumed to be governed by the incompressible, laminar, steady Navier–Stokes equations. Preliminary studies were performed to establish an appropriate multi-block grid configuration and spatial resolution.

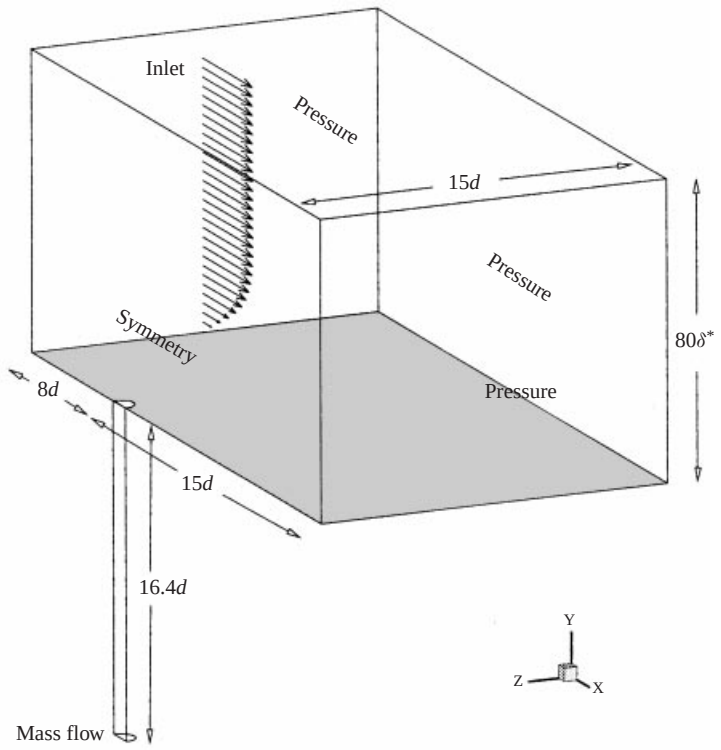

FIGURE 8. Schematic of a typical computational domain and boundary conditions used for an isolated perforation.

Case	d(mm)	U_e (m s^{-1})	L/d	d/δ^*	V_h/U_e	Re_{δ^*}	Suction	Principal features
I	1.0	12.2	16.4	0.77	0.50	1030	Sub-critical	Single vortex pair
II	1.3	16.1	12.6	1.05	1.02	1290	Super-critical	Two vortex pairs
III	0.8	16.2	20.4	0.68	2.00	1240	Super-critical	Two vortex pairs
IV	12.7	0.91	10.0	2.26	1.00	320	Super-critical	Unsteady vortex

TABLE 1. Details of validation test cases for the computational method.

6.2.1. *Computational domain*

The experimental boundary conditions were replicated as closely as possible by modelling the same geometry, by specifying identical ambient conditions, and by prescribing measured boundary layer velocity profiles on the inlet plane of the computational domain. Extensive preliminary studies were carried out to investigate the influence of the domain size and boundary conditions on the flow field. These investigations showed that the predicted induced flow field is symmetric around the perforation centreline and that identical results were obtained when symmetry boundary conditions were enforced along the symmetry plane. Figure 8 shows a schematic view of a typical computational domain and boundary conditions. The x, y and z coordinate axes are in the streamwise, surface-normal and lateral directions, respectively. To ensure that the Neumann boundary conditions did not have an erroneous influence on the predicted flow field the domain extended from $-8d$ to

$+15d$ longitudinally, $0d$ to $+12d$ laterally and from -16.32 mm up to $88\delta^*$ in the normal direction. As part of the experimental programme, for each free-stream speed employed, a datum three-dimensional boundary layer velocity profile was measured close to the perforation and with suction off. These measured profiles were used to specify the velocity distributions on the inlet plane, which was positioned far enough upstream to be independent of the influence of the suction hole. The remaining faces which complete the domain above the surface were set as pressure boundaries with uniform ambient pressure. The suction rate through the duct was specified by prescribing the mass flow rate at the duct outlet. Owing to the low free-stream and suction speeds involved ($U_e \approx 16\,\mathrm{m\,s^{-1}}$ and $V_h \approx 32\,\mathrm{m\,s^{-1}}$), an incompressible analysis was considered appropriate, and the ambient conditions were specified to match the wind tunnel environment.

6.2.2. *Computational grid*

The mesh size and density used depended on the expected flow features, based on the field measurements, and the resolution required to capture these flow field details. Consequently, owing to the variety of configurations investigated, and the desire to determine the flow features in as much detail as possible, the mesh size ranged between 180 000 and 530 000 cells. The grid was adjusted and tailored to provide high resolution through the boundary layer and in the regions where the trailing vortices occur.

6.3. *Single row of holes – time-dependent simulations*

Gregory (1962) performed low-speed smoke visualizations of the flow fields induced by both single and multiple rows of closely spaced (ratio of perforation pitch to diameter $s/d = 3$) large-scale ($d = 6.35$ mm and 12.7 mm) suction perforations in a thin flat plate. He investigated the effect of very strong suction on the laminar boundary layer with the ratio d/δ^* varying between 1.9 and 2.7, for free-stream speeds between $0.69\,\mathrm{m\,s^{-1}}$ and $0.91\,\mathrm{m\,s^{-1}}$. For a broad range of flow and geometric configurations he determined the critical suction velocity ratio, $(V_h/U_e)_{crit}$, and used smoke visualization to study the flow structures. With a single row of closely spaced perforations Gregory found that at low suction rates a pair of steady streamwise vortices was generated downstream of each perforation. At higher suction rates, however, the vortices of adjacent perforations were observed to link together transversely to form horseshoe vortex loops which detached periodically, were convected downstream and resulted in a rapid flow breakdown and transition to turbulence (figure 9). In contrast with most boundary layer flows, which are convectively unstable, the growth and shedding of these horseshoe vortices (leading to transition) may be an indication of absolute instability (Huerre & Monkewitz 1990). At even higher suction rates, the transverse vortices merged together to form steady 'standing' vortices between adjacent perforations and the flow became laminar again. Gregory measured the shedding frequency of the horseshoe vortices using a hot-wire probe.

As an additional validation test of the current prediction technique, one of Gregory's experimental configurations ($d = 12.7$ mm, $d/\delta^* = 2.26$, $U_e = 0.91\,\mathrm{m\,s^{-1}}$, $V_h/U_e = 1.00$, $s/d = 2.67$) was simulated here by generating a multi-block grid of the geometry and solving the incompressible, unsteady, Navier–Stokes equations. An implicit, time-centred Crank–Nicolson scheme was used to provide second-order accuracy for the time-stepping procedure. A time-dependent solution was generated by first obtaining a quasi-steady solution over coarse time steps followed by a series of smaller steps. This solution was then used as a starting point for further computations. The shedding

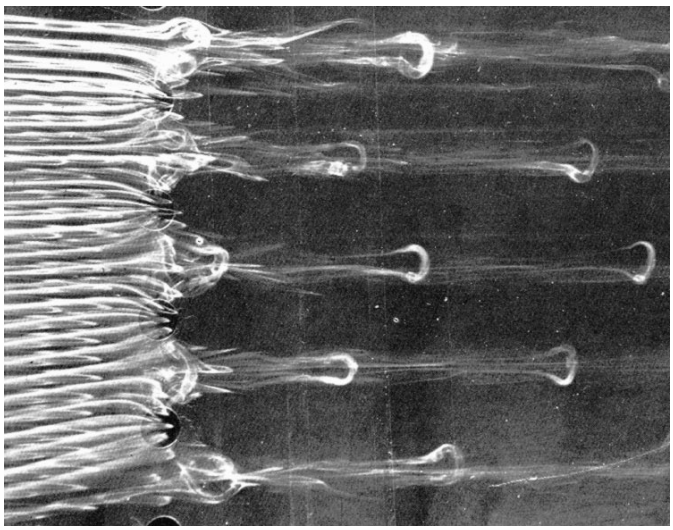

FIGURE 9. Smoke visualization of horseshoe vortices in a laminar boundary layer with suction applied through closely spaced perforations. Flow is from left to right (Gregory 1962).

frequency of the horseshoe vortices obtained from Gregory's smoke visualizations provides an initial estimate of the flow time scales. During the computational process the time steps were adjusted to the emerging solution until the resolution necessary to capture the unsteady features of the flow was established. In Gregory's experimental setup the disturbance sources that may influence the flow field included the free-stream turbulence levels, wind tunnel noise, suction pump oscillations and the flat plate roughness. It was impractical to include these effects in the simulation and they were therefore neglected. Also, the boundary conditions applied were steady.

6.3.1. *Computational domain*

The computational domain adopted for this simulation was topologically very similar to that developed for the isolated perforation cases described above. The primary difference was that in order to model a single transverse row of perforations the pressure boundary condition along the side of the domain (figure 8) was replaced by enforcing symmetry conditions. Gregory (1962) does not give a full description of the plate or of the suction system and the ratio of the perforation diameter to the perforation depth, L/d, he used is uncertain. From sketches of the experimental setup and some photographic evidence, it appears that a common plenum chamber was used to apply suction to the perforations and that the L/d ratio was less than 1. We suspect that this configuration resulted in sub-surface, inter-perforation effects. However, for want of detailed information, and to ensure that the outlet boundary assumptions are valid (Neumann conditions), L/d was set to 10 in the numerical model. In the experiment the super-scale perforations were closely spaced, and consequently the computational domain extended from $-8d$ to $+15d$ longitudinally, $0d$ to $+1.34d$ laterally and from $-10d$ to $55\delta^*$ in the normal direction.

6.3.2. *Boundary conditions*

The actual boundary layer velocity profile upstream of the suction perforations is also unknown, although the displacement thickness, δ^*, is given as 5.62 mm. As an approximation for simulation purposes, a steady-state Blasius profile, with the

same displacement thickness, was specified at the inlet plane (both U and V velocity components). Ambient conditions were specified on the remaining external domain faces and suction was applied by specifying a steady mass flow rate at the bottom of the perforation.

7. Comparison between predicted and measured flow fields

As noted in § 6, to validate the computational method four experimental configurations were simulated (table 1): three steady analyses, treating a range of configurations experimentally investigated here using an LDV, and one unsteady case, modelling the flow visualization experiment of Gregory (1962). The principal requirement of the computational technique is to predict the primary flow features and characteristics. Comparisons are now made between the predictions and measurements for isolated holes and single rows of super-scale perforations. In addition, the spatial resolution provided by the computational method permits a detailed analysis of the flow field which reveals the mechanism for the formation of the longitudinal vortex pairs.

7.1. *Isolated holes*

We found that the numerical method reproduced all of the primary flow features induced by a suction perforation and observed in the LDV measurements. Figures 10(*a*) and 10(*b*) compare the predicted and measured crossflow velocity vectors (V, W) in a plane $3d$ downstream of a perforation with super-critical suction applied. The data show that two pairs of co-rotating vortices appear aft of the perforation. As evident in figure 10*a*, the computations replicate these secondary, co-rotating vortices although they slightly under-predict their strength and extent. For a super-critical suction configuration (Case II), the predicted and measured U velocity contours on crossflow data planes are plotted in figures 11 and 12, respectively. The localized suction and induced streamwise vortices introduce strong distortions of the streamwise velocity. The localized thinning of the boundary layer is clearly evident in both the measurements and predictions and the spanwise extent of this region is bounded by the streamwise vortices. The vortex core spacing increases as the vortices progress downstream and the computations are in good agreement with the measurements.

Additional comparisons are made in figure 13 where the observed and predicted boundary layer velocity profiles along a surface curve defined by the vortex core are plotted. The longitudinal vortices introduce strong streamwise distortions which are reproduced, though again slightly underestimated, by the computations. Notice that at $1d$ downstream the numerical model properly predicts a region where the flow undergoes a complete reversal of direction.

The discrepancies between the predicted and measured results are most likely due to numerical dissipation and/or dispersion associated with the discretization of the convective terms. Numerical diffusion is a fundamental limitation of the computational method, and can only be improved by adopting a different discretization technique. It is anticipated that further improvement could be achieved by using a higher-order-accurate upwind scheme (Dacles-Mariani *et al.* 1995).

7.2. *Trailing vortex formation*

The mechanism for the formation of the streamwise vortex pairs may be examined by considering how the vorticity field is affected by the sink flow through the suction perforation. Although classical vortex kinematic theory assumes that the flow is

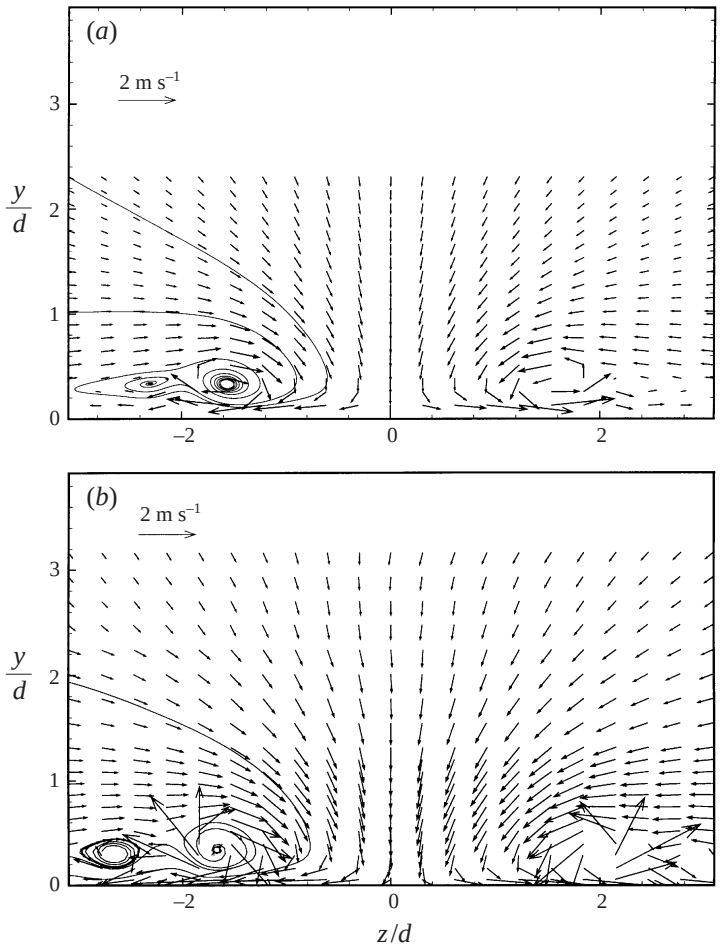

FIGURE 10. Looking upstream, V, W crossflow velocity vectors $3d$ downstream of an isolated suction perforation: (*a*) computed (*b*) measured. Secondary vortices are highlighted using two-dimensional streamtraces (Case II: $d = 1.3\,\text{mm}$, $d/\delta^* = 1.05$, $V_h/U_e = 1.02$).

inviscid, barotropic and only subject to potential body forces (Green 1995), it offers a useful vehicle for exploring the inception and development of the streamwise vortices observed here. Given the above assumptions, Kelvin's Theorem (or Helmholtz's second law of vortex motion) states that vortex lines are the same as material lines which are convected with the local fluid velocity. For the current simulations, the material lines were determined by first calculating the time-dependent locations of fluid particles which were 'released' along a transverse line at a uniform height within the boundary layer, and subsequently by assembling isochronous particle locations to generate material (or time) lines. For discussion purposes we will now refer to these computed lines as vortex lines. Figure 14 shows a sample set of vortex lines, drawn at uniform time intervals, for an isolated super-scale perforation with sub-critical suction applied ($d = 1.0\,\text{mm}$, $d/\delta^* = 0.77$, $V_h/U_e = 0.50$); the fluid particles were initially released at $y/\delta^* = 0.14$.

To analyse the formation of the pair of trailing vortices, we first follow the activity of an individual vortex line during its passage through the domain. Far upstream

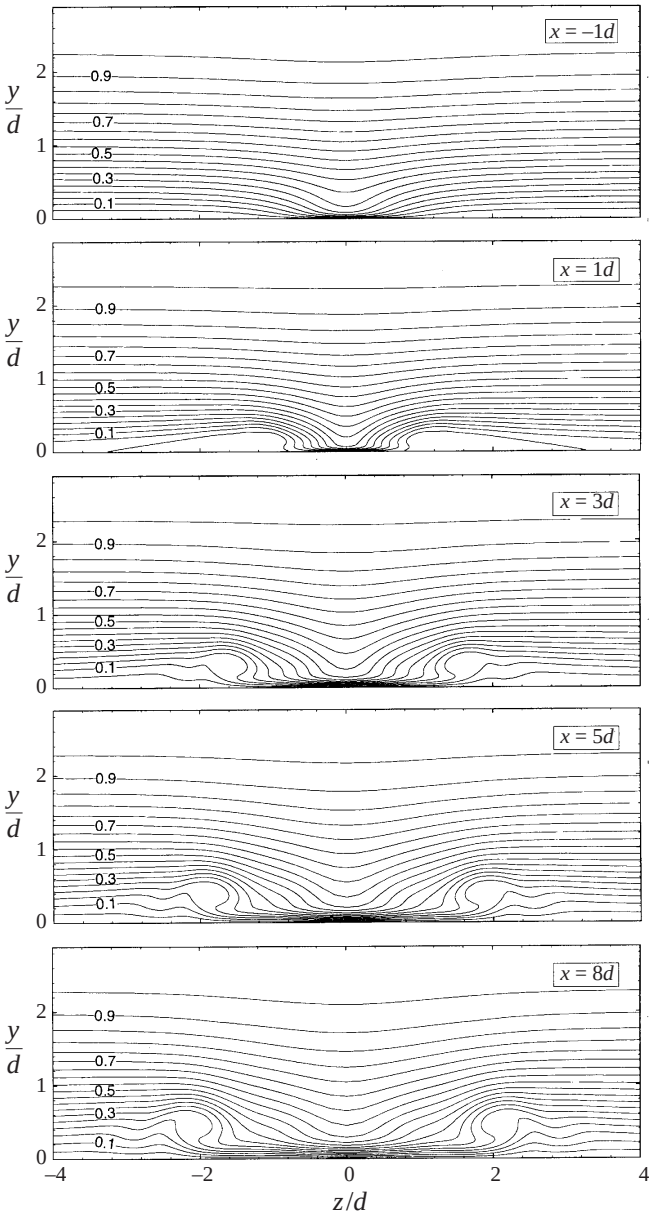

FIGURE 11. Sequence of predicted contours of streamwise velocity, U/U_e, in crossflow data planes upstream and downstream of an isolated perforation with super-critical suction applied: (Case II: $d = 1.3$ mm, $d/\delta^* = 1.05$, $V_h/U_e = 1.02$).

of the suction perforation the vortex line is effectively unperturbed and therefore straight and normal to the velocity vectors (A–A′). As it comes under the influence of the sink flow entering the suction perforation, the centrepoint of the vortex line is pulled forward and the line deforms (B–B′). After being ingested into the perforation duct, the vortex line folds tightly in two about its centrepoint to form a pair of vortex filaments; viewed along the duct axis these filaments rotate in opposite senses to one another (figure 15). Meanwhile, towards the side boundries in the exterior flow, the

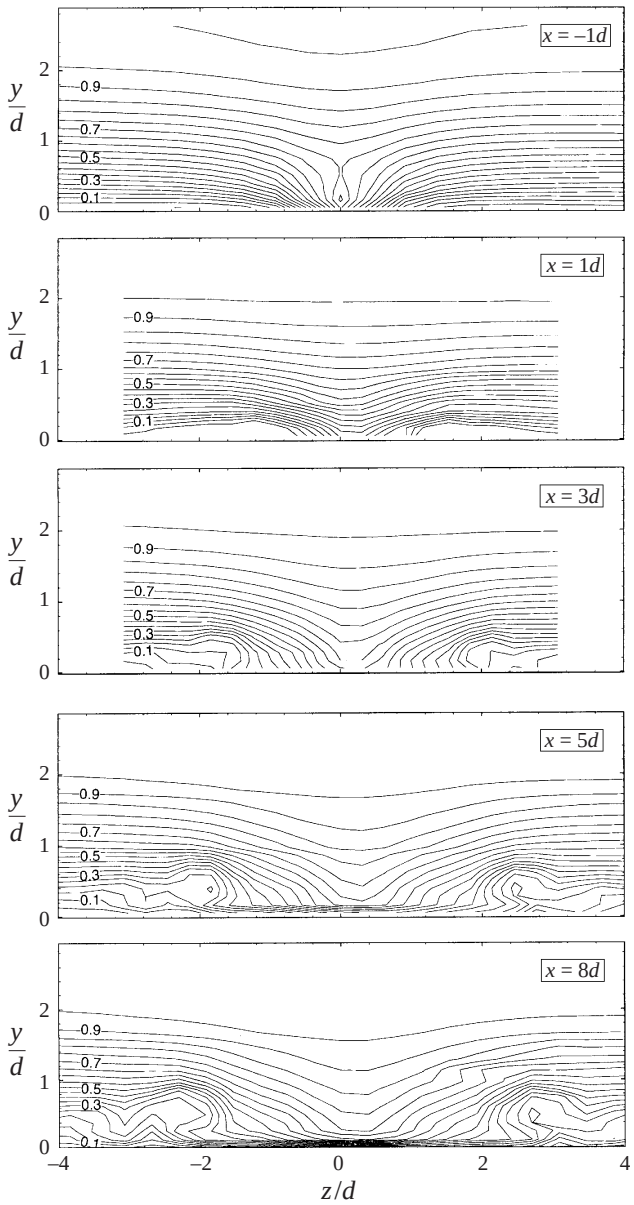

FIGURE 12. Sequence of measured contours of streamwise velocity, U/U_e, in crossflow data planes upstream and downstream of an isolated perforation with super-critical suction applied: (Case II: $d = 1.3$ mm, $d/\delta^* = 1.05$, $V_h/U_e = 1.02$).

extremities of the (now divided) filaments remain aligned with their initial directions. Close to the centreline the filament bends sharply upstream (C–C′), and is being stretched, thus increasing its vorticity. Stretching is clearly evident in the exterior flow, but of course also occurs within the duct. For successive positions of the attached vortex lines it can be seen that the inner segments coalesce to form a pair of smooth curves emanating from the suction perforation. If we now regard figure 14 as an instantaneous view of a set of discrete vortex lines, we can visualize how the inner

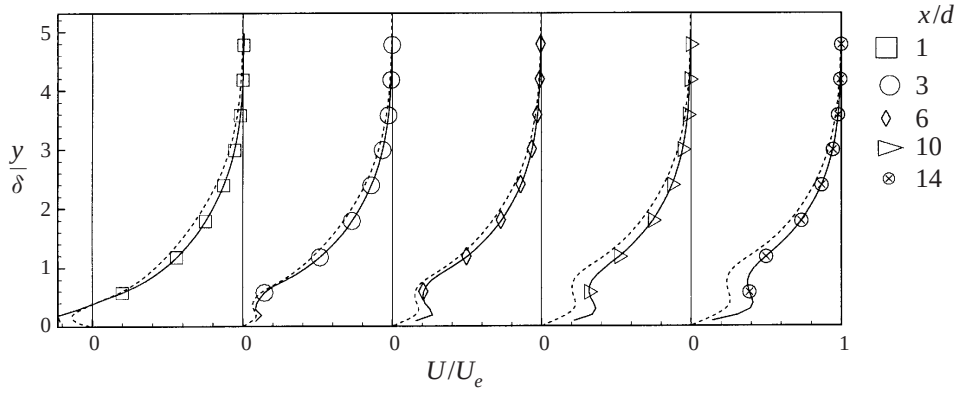

FIGURE 13. Measured (solid lines) and computed (dotted lines) U/U_e velocity boundary layer profiles at different positions along the path of the vortex core (Case III: $d = 0.8$ mm, $d/\delta^* = 0.68$, $V_h/U_e = 2.00$). Approximately every seventh measurement point is shown.

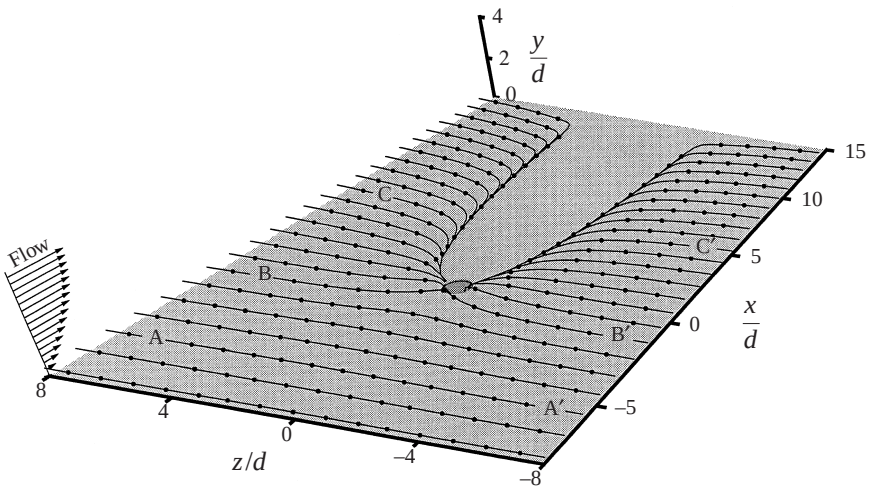

FIGURE 14. Calculated boundary layer material lines illustrating the formation of streamwise vortices downstream of a suction perforation (Case I: $d = 1.0$ mm, $d/\delta^* = 0.77$, $V_h/U_e = 0.50$). Approximately every tenth particle location is shown.

segments of the lines are co-aligned and amalgamate to create a pair of concentrated trailing vortices. Viscosity causes the vortex cores to diffuse, thus the peak level of vorticity depends on the balance between the vorticity amplification due to stretching and the attenuation due to viscous effects.

For these cases the maximum vorticity appears at the downstream lip of the hole inlet on each side of the symmetry plane (at an angle of about $\pm 45^\circ$ from the hole centre between the streamwise and lateral directions). Although vorticity is enhanced by compressibility effects (Green 1995) the local flow field of a micro-perforation under transonic flight conditions has been shown to be insensitive to compressibility (MacManus 1997). This brief analysis outlines the principal issues concerned with vortex formation and establishes the mechanism by which the suction hole generates longitudinal vortices.

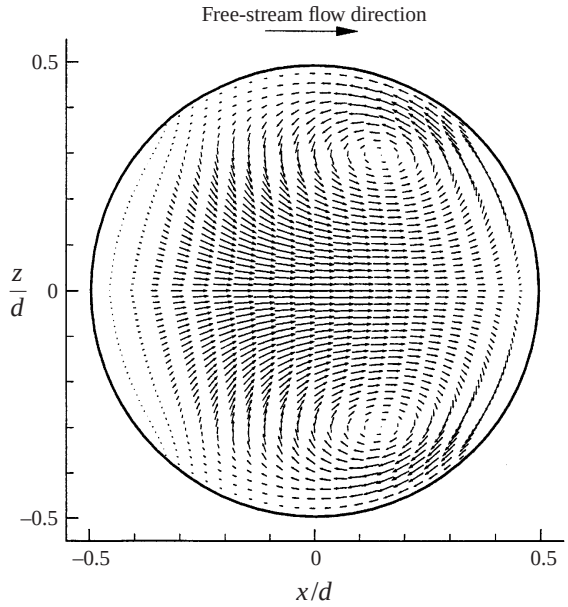

FIGURE 15. Velocity vectors in the (x, z)-plane, $0.25d$ below the surface, showing the pair of contra-rotating vortices in the suction duct (Case I: $d = 1.0$ mm, $d/\delta^* = 0.77$, $V_h/U_e = 0.50$).

7.3. *Single row of perforations – unsteady analyses*

In accordance with the experimental observations of Gregory and Goldsmith (figure 9), instead of the steady longitudinal vortices that occur downstream of closely spaced suction perforations, the computations predict an unstable cross-stream vortex link between adjacent perforations. This lateral vortex is periodically shed and convected downstream. For the suction velocity ratio applied in this simulation ($V_h/U_e = 1.0$) the vortex is found to be unsteady and time-dependent flow structures are observed downstream of the row of perforations. The temporal evolution and spatial progression of these vortical regions are illustrated in figure 16 where the contours of lateral vorticity ($\Omega_z^* = \Omega_z \delta^*/U_e$) in the symmetry plane (i.e. equidistant between adjacent perforations) are shown. The lateral vorticity at every second time step between $t/\Delta t = 450.3$ and 462.3 is plotted. These predictions indicate that the detachment of the primary vortex is followed by a series of secondary vorticity bursts. In figure 16, the progressions of specific vortical features through the time steps are indicated with a dashed line.

Analysis of the predicted velocity time traces over 54 time steps shows that the primary vortex shedding frequency, f_1, is approximately 2.8 Hz, corresponding to a Strouhal number ($f_1 d/U_e$) of 0.04. This is a factor of 2.3 times less than the vortex shedding frequency measured by Gregory (1962) using a hot-wire probe. The differences between the predicted and measured flow fields are probably due to the dissimilar sub-surface configurations and to the exclusion of the experimental disturbance environment from the computations. These results emphasize the need to preserve the dimensionless perforation parameters (e.g. L/d) when performing HLFC experiments. The predicted velocity time histories at a range of loci within the domain were extracted and power spectral analyses of these indicate that the flow field is dominated by three well-defined frequencies of equal power. The Strouhal numbers for these frequencies are estimated as 0.04, 0.08 and 0.12, which correspond to the fundamental and the first and second sub-harmonics.

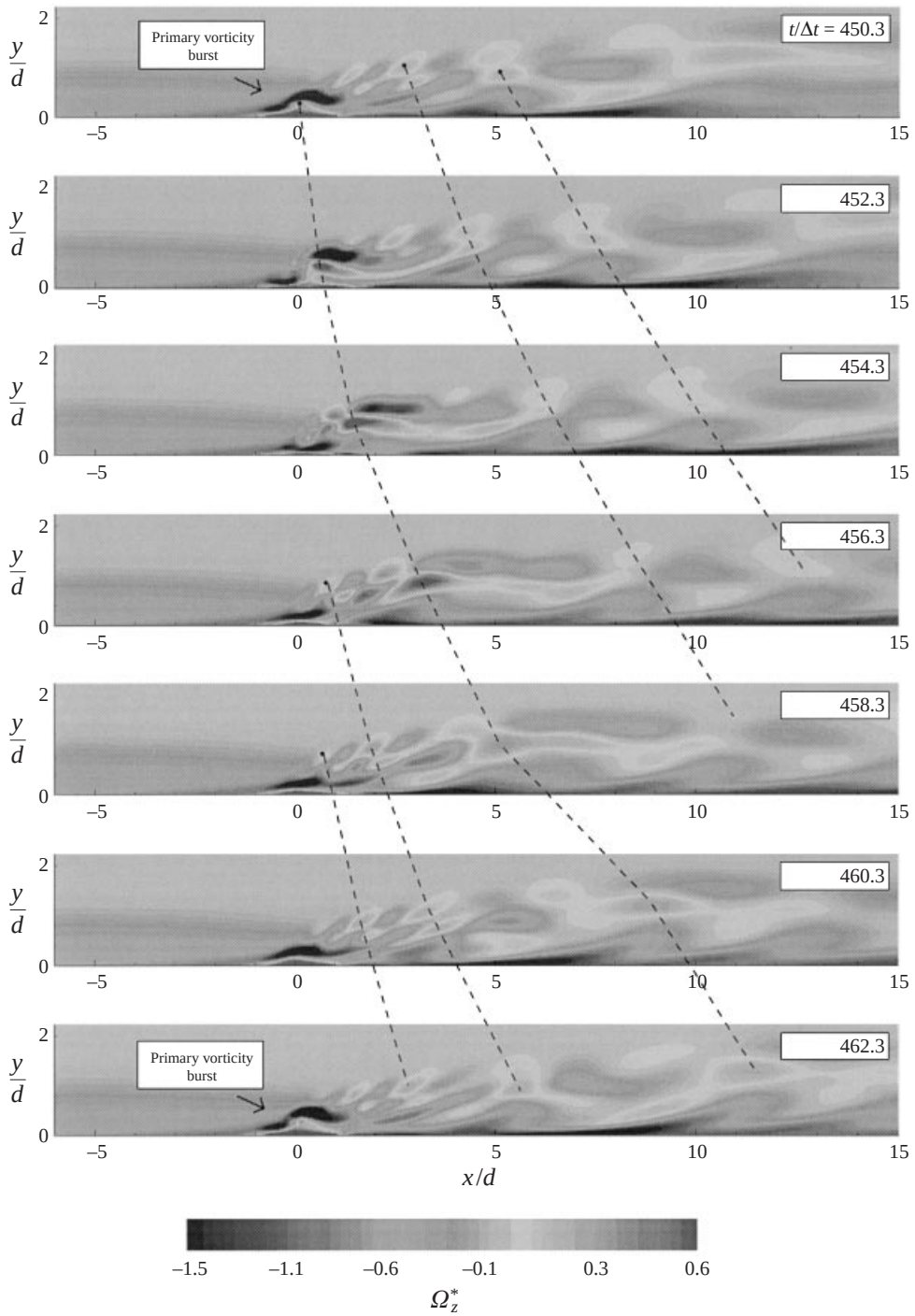

FIGURE 16. Time sequence of contours of lateral vorticity, Ω_z^*, in the (x, y) symmetry plane over seven time steps (Case IV: $d/\delta^* = 2.26$, $V_h/U_e = 1.00$, $Re_{\delta^*} = 320$).

8. Application of the numerical method

Sections 3–5 describe the development and application of a measurement technique to study the detailed flow fields of isolated, super-scale HLFC suction perforations under low-speed conditions. These measurements show that the application of discrete suction through perforations introduces a range of complex flow phenomena into the laminar boundary layer and produces a flow field that is fundamentally different from the idealized concept of continuously distributed suction. It is also known that some of these suction-induced features strongly affect the boundary layer behaviour and may expedite the transition process under particular conditions.

In § 7 a computational method was developed and validated by simulating a range of super-scale, low-speed flow field experiments. Comparisons between the computational and experimental results show that the numerical method reproduces all of the primary flow features induced in a laminar boundary layer by a super-scale suction perforation. Considering the present impossibility of performing detailed flow measurements on true-scale micro-perforations under transonic conditions, the current low-speed experiments have provided a suitable set of validation test cases.

As discussed in § 1 the establishment of design criteria for HLFC suction surfaces requires detailed knowledge of the flow fields induced by micro-scale perforations under transonic flight conditions where compressibility, scale, and inter-hole effects may be significant. In addition, many previous fundamental investigations of HLFC suction surfaces have been performed using micro-scale perforations under low-speed wind-tunnel conditions (Saric & Reed 1986; Poll, Danks & Davies 1992). With these studies, however, similarity was not preserved and, as highlighted in § 5.1, the suction-induced flow field is particularly sensitive to d/δ^*, for example. Consequently, the current computational method has been applied to a wide range of practical problems including the analysis of micro-scale perforations under lower-speed wind-tunnel conditions as well as single and multiple row configurations of actual-size holes under transonic flight conditions. A detailed account of these analyses is given by MacManus (1997) and only some limited highlights are presented here.

8.1. *Single row of micro-perforations – flight cruise conditions*

It was found (MacManus & Eaton 1996*a*; MacManus 1997) that the flow field induced by a single row of micro-perforations under transonic conditions is characteristically the same as that measured in the low-speed experiment where similarity has been preserved. Two longitudinal vortices are generated downstream of each suction perforation and the level of induced streamwise vorticity increases with increasing V_h/U_e, d/δ^* and when the perforation is inclined into or away from the flow direction. The flow field in the vicinity of the perforation inlet is found to be of a highly three-dimensional nature with contra-rotating vortices positioned along the duct axis which demonstrate that, when numerically (or experimentally) modelling a HLFC suction surface, it is necessary to preserve the length to diameter ratio, L/d.

To avoid premature transitioning of the boundary layer it is vital that outflow is avoided at all points along the suction surface. This requires an accurate estimate of the pressure losses through the surface and the transonic simulations reveal that the pressure drop is highly dependent on the presence of a grazing flow, d/δ^* and on the suction hole geometry (MacManus & Eaton 1996*a*). Also, comparisons with the current engineering design criteria show that the pressure losses are significantly underestimated, thereby running the risk of outflow occurring. The effect of compressibility on the suction-induced flow features was assessed and found to be very

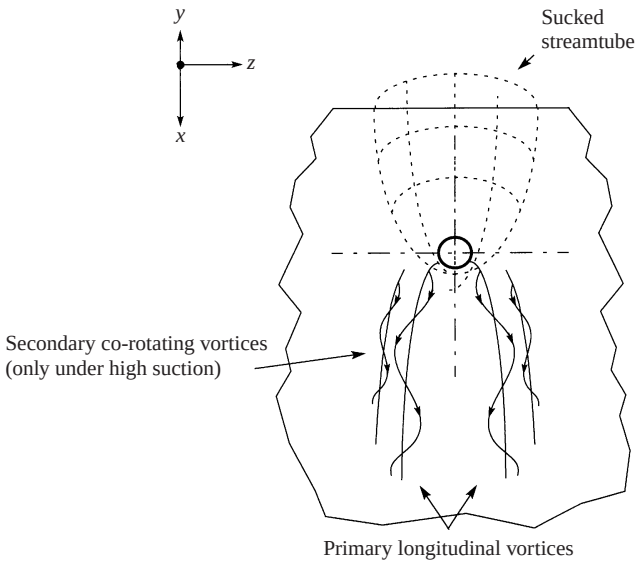

FIGURE 17. Isolated, super-scale perforation under low-speed conditions.

minor. Predictions for multiple rows of micro-perforations reveal that there are strong inter-hole effects and that the induced vorticity increases with each successive row of holes.

8.2. *Single row of micro-perforations – low-speed conditions*

Analysis of the simulations of micro-scale perforations under low-speed conditions revealed that the suction-induced flow field was markedly different from that of a typical HLFC suction surface under flight conditions. The characteristic longitudinal vortices were not predicted and the sucked streamtube now extended between adjacent holes, thereby removing all the boundary layer below a certain height. In addition, another flow mode was identified for a configuration corresponding to an experiment where over-suction induced transition was observed (MacManus 1997). In this case a pair of widely spaced, co-rotating longitudinal vortices was observed to commence approximately $3d$ downstream of the perforation and close to the side symmetry plane. In the light of these differences, considerable caution is advised when drawing conclusions from, or basing design criteria on, low-speed experiments where dynamic similarity has not been preserved.

8.3. *Flow field modes induced by discrete suction – pictorial summary*

A broad range of suction surface configurations has been both experimentally and computationally investigated. A wide variety of suction-induced flow phenomena have been observed and the flow mode was found to depend on the boundary layer characteristics, the suction level and the perforation geometry and configuration. To emphasize the complexity of such seemingly simple and innocuous flow configurations, a pictoral summary, in the form of a sequence of cartoons of the different flow field modes induced by discrete suction through perforations is presented in figures 17–22.

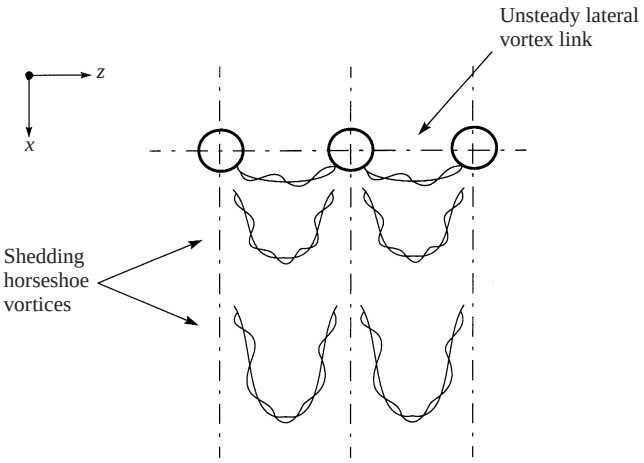

FIGURE 18. Single row of closely spaced, super-scale perforations under low-speed, high-suction conditions.

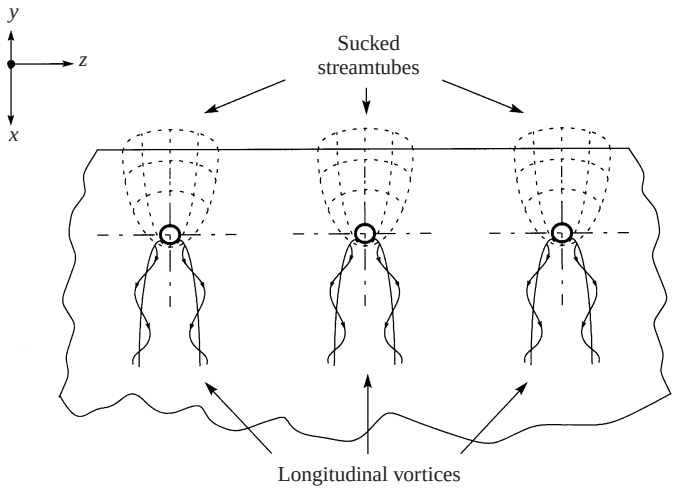

FIGURE 19. Single row of micro-perforations under typical transonic flight conditions.

9. Critical suction parameters

As discussed in § 1 knowledge of the critical suction limits is of vital importance to the successful design of HLFC suction surfaces and a variety of design criteria have been previously suggested (Goldsmith 1957; Pfenninger 1977; Reneaux & Blanchard 1992; Ellis & Poll 1996). These methods include a critical hole Reynolds number and a variety of equivalent roughness analogies. Previous workers have drawn parallels between the flow field induced by suction perforations and those of isolated three-dimensional roughness elements, which have received considerable attention (Gregory & Walker 1950; Tani 1961, 1981; Schlichting 1968; Acarlar & Smith 1987; Klebanoff, Cleveland & Tidstom 1992). It has been suggested that the size of the sucked streamtube envelope (figure 1) has a similar effect to that of a roughness element, for which many data are available. Blanchard *et al.* (1991) proposed a critical equivalent roughness parameter which assumes a rectangular cross-sectional shape for the sucked streamtube and then uses the known suction mass flow and a predicted boundary

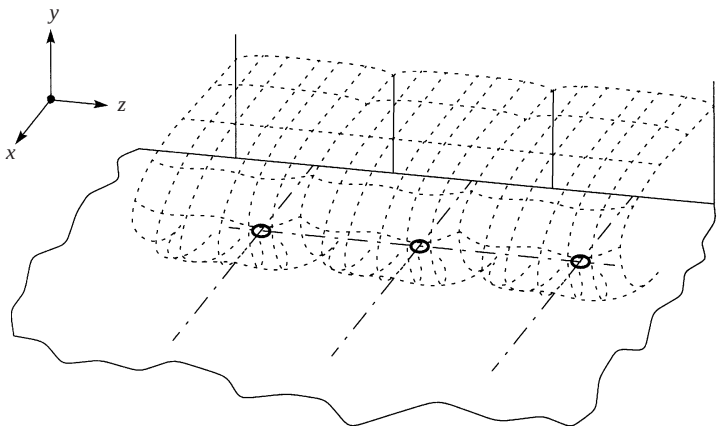

FIGURE 20. Single row of micro-perforations under low-speed, wind tunnel conditions (very low d/δ^*).

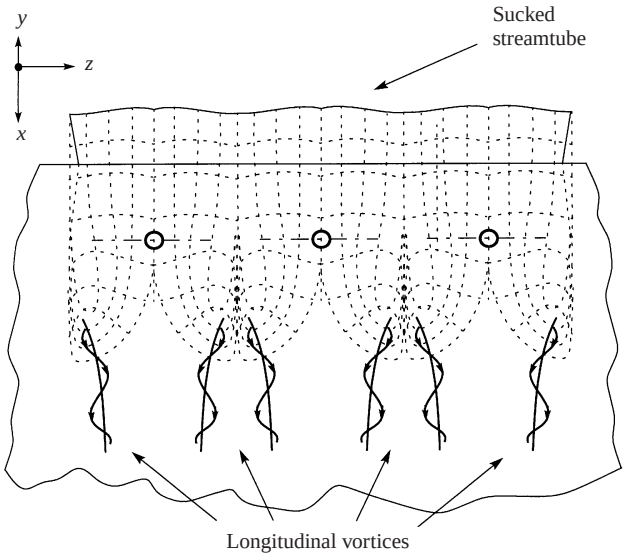

FIGURE 21. Single row of micro-perforations under low-speed, wind tunnel conditions with over-suction applied (very low d/δ^*).

layer profile to estimate the height of the sucked streamtube. This is then used in an empirical correlation to predict the critical suction velocity. The detailed experimental flow-field mappings, low-speed simulations and flight condition predictions described here offer an unique opportunity to discover the detailed characteristics of the sucked streamtube and to extract a practical engineering design criterion for the critical suction limit. Only a brief outline of the principal results are presented here and further details are available in MacManus (1997), and MacManus & Eaton (1998).

The sucked streamtube is the envelope containing all of the fluid ingested by the suction perforation and, following Goldsmith (1957), it is schematically illustrated in figure 1. The current flow field measurements and predictions have been used to determine, for the first time, the actual shape and size of the sucked streamtube envelope and it has been shown (MacManus 1997) that the typical assumption of a

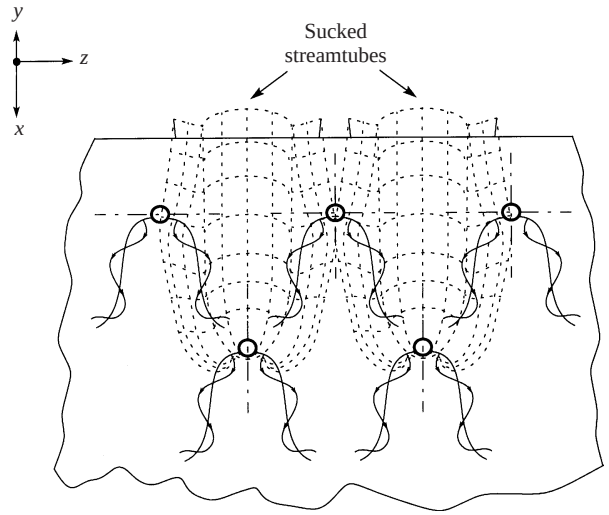

FIGURE 22. Multiple rows of micro-perforations under typical transonic, flight conditions.

rectangular streamtube is unrealistic and inaccurate. The suction envelope topology suggested by Goldsmith was found to be more realistic and the approach of relating known flow quantities to a streamtube Reynolds number, $Re_k = U_k y_k / \nu$ (where y_k is the height of the sucked streamtube and U_k is the streamwise velocity at this height) has been adopted here. As presented by MacManus & Eaton (1998), analysis of the low-speed experiments and associated simulations shows that Goldsmith's parameter, $G_k = (1/\nu) Q_h^{2/3} (\partial U / \partial y)^{1/3}$, captures the characteristics of the sucked streamtube and results in a simple critical suction criterion ($G_{k_{crit}} = 740$). Q_h is defined as the volume flow rate through the suction perforation.

Considering this success of Goldsmith's parameter in determining a low-speed critical suction parameter, the analysis has also been extended to include the predictions of single and multiple rows of micro-perforations under flight conditions. The objective of this analysis is to determine whether a simple relationship exists between Goldsmith's parameter (derived from quantities known to the designer) and the detailed characteristics of the sucked streamtube (accessible only through micro-scale simulations). Figure 23 shows the variation of the predicted streamtube Reynolds number, Re_k, with Goldsmith's parameter, G_k, for a wide variety of configurations. Although some scatter occurs in the results, there is a reasonably linear relationship between Re_k and G_k. This is similar to the low-speed results (MacManus 1997) and, although there is clearly a need for further experimental data, it indicates that Goldsmith's parameter, G_k, is also pertinent to HLFC suction surfaces under flight conditions.

10. Conclusions

Fundamental insights into the flow physics of HLFC suction surfaces were obtained by conducting a coordinated series of experimental and computational investigations. An unique set of high-resolution three-dimensional experiments was performed to non-intrusively measure, in detail, the flow field induced in a laminar boundary layer by suction through isolated perforations. The measurements confirm that these flows are strongly three-dimensional in nature. A broad range of suction-induced flow phenomena were observed, including a pair of streamwise vortices, multiple

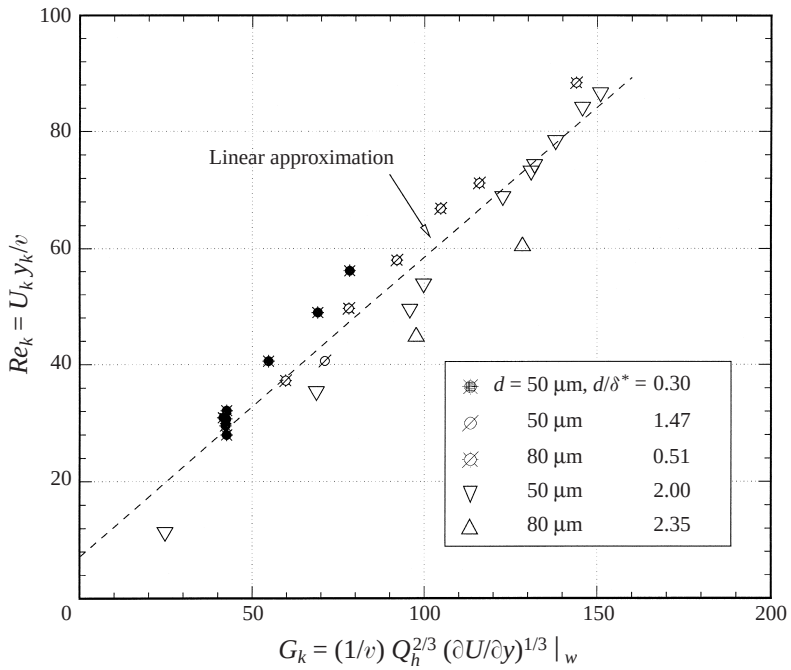

FIGURE 23. Predicted variation of Re_k with Goldsmith's parameter, G_k, for single and multiple rows of micro-perforations under transonic, flight conditions.

co-rotating vortices, distortions of the streamwise velocity distribution and inherently unstable velocity profiles. Surveys of the r.m.s. velocity in planes parallel to the surface show that suction-induced transition is a gradual process which results in the development of two turbulent wedges downstream of the suction perforation. This discovery reveals that suction-induced transition is precipitated through instabilities of the streamwise vortices. The critical suction velocity ratio for isolated perforations, over a range of d/δ^*, was determined and the critical suction limit was found to be inversely dependent on d/δ^*. An important finding is that as the relative diameter of the perforation is reduced, there appears to be a limiting diameter ($d/\delta^* \approx 0.6$) below which suction will not provoke transition.

In parallel with these experiments, a computational method was developed for predicting the detailed laminar flow fields of HLFC suction surfaces. This numerical method was validated by modelling the low-speed experimental configurations and comparisons between the measurements and predictions show that the numerical method reproduces all of the primary flow features induced in a laminar boundary layer by a suction perforation. The predictions, however, slightly underestimate the extent and magnitude of the phenomena, most likely because of numerical diffusion effects. Analysis of the computational results shows that the formation of the longitudinal vortices results from stretching and reorientation of the material lines. The computational technique was also successfully used to simulate flow visualization experiments of a single transverse row of closely spaced perforations, where an unsteady lateral vortex between adjacent perforations was found to be shed periodically downstream.

In addition, the computational method, now validated for low-speed cases, was applied to a range of typical flight and low-speed configurations. Overall, a wide

range of flow field modes and phenomena were identified and both the experiments and predictions revealed that the suction-induced flow is profoundly different from the idealized concept of continuously distributed suction. A critical suction design criterion, based on the measured and predicted sucked streamtube characteristics, was established for low-speed configurations and the basis of this criterion was assessed in relation to single and multiple rows of micro-perforations under flight conditions.

This work was supported in part by the Commission of the European Communities Industrial and Materials Technology (Aeronautics) program, under the European Laminar Flow Investigation (ELFIN II) project. The experimental work was funded by Airbus Industrie and the authors thank Joachim Szodruch, Robert Hinsinger and Daniel Arnal for their support. We are grateful to the staff in the Department of Aerospace Engineering at the University of Bristol who made their facilities available and assisted with the experiments. Figure 10 was provided courtesy of Peter Bradshaw and Jonathan Morrison.

REFERENCES

Acarlar, M. & Smith, C. 1987 A study of hairpin vortices in a laminar boundary layer, Part 1. *J. Fluid Mech.* **175**, 1–41.

Arnal, D. 1992 Boundary layer transition: prediction, application to drag reduction. *AGARD Rep.* 786, pp. 5.1–5.59.

Barrett, R. 1984 Design and performance of a new low turbulence wind tunnel at Bristol University. *RAeS Aero. J.* 86–90.

Barrett, R., Rickards, J., Swales, C. & Brake, C. 1993 Enhanced performance of a cross-coupled 3D laser Doppler anemometer for small scale flow surveys using improved alignment and operational procedures. In *Proc. Intl Congress on Instrumentation in Aerospace Simulation Facilities.* IEEE.

Blanchard, A., Seraudie, A., Breil, J. & Payry, M. 1991 Limits of suction through a perforated metal sheet on a model to avoid transition tripping. *ONERA-DERAT Rep.* 38/5006.21, Toulouse, France.

Braslow, A. & Fischer, M. 1984 Design considerations for the application of laminar flow control systems to transport aircraft. *AGARD CP 365*, pp. 4.1–4.27.

CFDS 1994 *FLOW3D Release 3.3 User Manual.* Computational Fluid Dynamics Services, AEA Technology, Harwell, UK.

Dacles Mariani, J., Zilliac, G., Chow, J. & Bradshaw, P. 1995 Numerical/experimental study of a wingtip vortex in the near field. *AIAA J.* **33**, 1561–1568.

Ellis, J. & Poll, D. 1995 Laminar and laminarizing boundary layers by suction through perforated plates. In *Proc. 2nd CEAS European Forum on Laminar Flow Technology, Bordeaux, France.*

Goldsmith, J. 1957 Critical laminar suction parameters for suction into an isolated perforation or a single row of holes. *Northrop Aircraft Inc. Rep.* BLC-95.

Green, S. 1995 *Fluid Vortices.* Kluwer.

Gregory, N. 1961 Research on suction surfaces for laminar flow. In *Boundary Layer and Flow Control* (ed. G. V. Lachmann), vol. 2, pp. 924–960. Pergamon.

Gregory, N. 1962 On critical suction conditions for laminar boundary-layer control by suction in perforations. *Aero. Res. Counc. Rep.* 24, 213.

Gregory, N. & Walker, W. 1950 The effect on transition of isolated surface excressences in the boundary layer. *Aero. Res. Counc. Rep.* 13436 (also *Aero. Res. Counc. R. & M.* 2799, 1951).

Herbert, T. 1988 Secondary instability of boundary layers. *Ann. Rev. Fluid Mech.* **20**, 487–526.

Holmes, B. 1987*a* A historical review of LFC for aircraft. In *Applied Viscous Control for Drag Reduction.* University of Kansas.

Holmes, B. 1987*b* NLF design and applications considerations. In *Applied Viscous Control for Drag Reduction.* University of Kansas.

Huerre, P. & Monkewitz, P. 1990 Local and global instabilities in spatially developing flows. *Ann. Rev. Fluid Mech.* **22**, 473–537.

KLEBANOFF, B., CLEVELAND, W. & TIDSTOM, K. 1992 On the evolution of a turbulent boundary layer induced by a three-dimensional roughness element. *J. Fluid Mech.* **237**, 101–187.

LEONARD, B. 1979 A stable and accurate convective modelling procedure based on quadratic upstream interpolation. *Comp. Meth. Appl. Mech. Engng* **19**, 59–98.

MACMANUS, D. 1997 An aerodynamic prediction technique for laminar flow control suction surfaces. PhD thesis, National University of Ireland.

MACMANUS, D. & EATON, J. 1996*a* Micro-scale, three-dimensional Navier–Stokes investigation of laminar flow control suction perforation configurations. *AIAA Paper* 96-0544.

MACMANUS, D. & EATON, J. 1996*b* Predictions and observations of the flow field induced by laminar flow control micro-perforations. *Expl Thermal Fluid Sci.* **13**, 395–407.

MACMANUS, D. & EATON, J. 1998 Measurement and analysis of the flowfields induced by suction perforations. *AIAA J.* **36**, 1553–1561.

MACMANUS, D., EATON, J., BARRETT, R., RICKARDS, J. & SWALES, C. 1996 Mapping the flow field induced by a HLFC perforation using a high resolution LDV. *AIAA Paper* 96-0094.

MEYER, W. 1955 Preliminary report on the flow field due to laminar suction through holes. *Rep.* BLC-75. Northrop Aircraft Inc., Hawthorne, California.

MORKOVIN, M. 1978 Instability, transition to turbulence and predictability. *AGARDograph* 236.

NAYFEH, A. 1981 Effect of streamwise vortices on Tollmien-Schlichting waves. *J. Fluid Mech.* **107**, 441–453.

PFENNINGER, W. 1977 Laminar flow control laminarisation. *AGARD Rep.* 654, pp. 3.1–3.43.

POLL, D., DANKS, M. & DAVIES, A. 1992 The effect of surface suction near the leading edge of a swept-back wing. In *Proc. 1st CEAS European Forum on Laminar Flow Technology, Hamburg, Germany*.

REED, H. & SARIC, W. 1989 Stability of three-dimensional boundary layers. *Ann. Rev. Fluid Mech.* **21**, 235–284.

RENEAUX, J. & BLANCHARD, A. 1992 The design and testing of an airfoil with hybrid laminar flow control. In *Proc. 1st CEAS European Forum on Laminar Flow Technology, Hamburg, Germany*.

RHIE, C. & CHOW, W. 1983 Numerical study of the turbulent flow past an airfoil with trailing edge separation. *AIAA J.* **21**, 1527–1532.

SARIC, W. 1985 Laminar flow control with suction: theory and experiment. *AGARD Rep.* 723, pp. 3.1–3.11.

SARIC, W. & REED, H. 1986 Effect of suction and weak mass injection on boundary layer transition. *AIAA J.* **24**, 383–389.

SCHLICHTING, H. 1968 *Boundary Layer Theory*. McGraw-Hill.

TANI, I. 1961 Effect of a two-dimensional and isolated roughness on laminar flow. In *Boundary Layer and Flow Control* (ed. G. V. Lachmann), vol. 2, pp. 637–656. Pergamon.

TANI, I. 1981 Three-dimensional aspects of boundary layer transition. *Proc. Indian Acad. Sci.* **4**, 219–238.

VAN DOORMAL, J. & RAITHBY, C. 1984 Enhancement of the SIMPLE method for predicting incompressible fluid flows. *Numer. Heat Transfer* **7**, 147–163.